Fabrication of 1D/3D heterostructure perovskite layers by tetrabutylammonium tetrafluoroborate for high-performance devices

Seid Yimer Abate[a], *Surabhi Jha*[b], *Abdul Kalam Shaik*[c], *Guorong Ma*[b], Jada Emodogo[a], *Nihar Pradhan*[a], *Xiaodan Gu*[b], *Derek Patton*[b], *Nathan I. Hammer*[c], *Qilin Dai*[a*]

[a] *Department of Chemistry, Physics, and Atmospheric Sciences, Jackson State University, Jackson, MS, 39217, United States*

[b] *School of Polymer Science and Engineering, Center for Optoelectronic Materials and Devices, The University of Southern Mississippi, Hattiesburg, MS, 39406, United States.*

[c] *Department of Chemistry and Biochemistry, The University of Mississippi, University, MS, 38677, United States.*

*Corresponding author: Q. Dai, Email: qilin.dai@jsums.edu

Abstract

Organic-inorganic halide perovskites achieved tremendous success in solar cells, however, their commercialization has not yet been realized. The primary reason is the intrinsic property of perovskite film. The significant density of defects in the polycrystalline perovskite layers influenced not only the performance of the solar cell as well its long-term stability. Here, we employed a post-surface treatment of the perovskite layer by tetrabutylammonium tetrafluoroborate (TBATFB). TBATFB interacted through hydrogen bonding with the 3D perovskite and formed an in situ a 1D $TBAPbI_{1.66}Br_{0.34}BF_4$ on the surface of the 3D perovskite. This low-dimensional 1D perovskite (perovskitoid) capping layer represses the defects in perovskite by blocking the nonradiative recombination centers and minimizing the surface and grain boundary defects. Our experimental results verified both the electron and hole defects were significantly suppressed by the TBATFB modification. As a result, the 1D/3D heterostructure device exhibited a champion performance of 21.68% PCE compared to 20.03% PCE for the control device. Intriguingly, the 1D TBAPbI$_{1.66}$Br$_{0.34}$BF$_4$ capping layer safeguards the 3D perovskite from the infiltration of moisture thus the TBATFB modified devices maintained 99% of their initial performance after 720h in the air (RH=40-60%).

Keywords

Surface passivation, tetrabutylammonium tetrafluoroborate, perovskitoid, 1D/3D heterostructure, perovskite solar cells

Introduction

The performance of perovskite solar cells is tremendously increased from 3.8% to above 26%[1] in decades and many investigations are onwards to realize the commercialization of such devices, however, the bottleneck challenge is still there. One of the primary challenges is the large density of defects in the polycrystalline perovskite layer. The organic-inorganic halide perovskite has a general formula of ABX$_3$, where A is a cation such as MA$^+$, FA$^+$ and Cs$^+$; B is a bivalent metal (Pb^{2+}); and X is halogens (Cl$^-$, Br$^-$, I$^-$). The perovskite structure is formed by the interaction between the A cations with the cationic-anionic octahedra [BX$_6^{4-}$] through electrostatic interactions and weak hydrogen bonding.[3] Therefore, under various stimuli such as electric field, illumination and/or temperature the charged constituents of the perovskite could mobile and displaced from their original lattice sites, consequently, defects formed in the perovskite. Moreover, in the solution-processed perovskite films the crystal-growth kinetic is fast, as a result, polycrystalline films formed, which caused various structural defects.[4] In general, perovskite defects are shallow-level due to their low formation energy and the defects could be halide vacancies, cation vacancies, anti-site defects, and interstitial defects. The halide vacancies resulted undercoordinated positively charged Pb^{2+} ions, and the cation vacancies create undercoordinated negatively charged I^- ions and/or PbI_3^- anti-sites.

These electronic defects influenced the charge transport and extraction by trapping/de-trapping charge carriers. Such defects serve as a non-radiative charge recombination center consequently the photoluminescence of the perovskite film diminishes. The device prepared with such perovskite films shows mediocre V_{oc} and FF. Besides, such traps influence the device parameters when the device operated under the forward bias or reverse bias, consequently, they aggravated hysteresis. Moreover, the surface and grain boundary defects are the main reason for device degradation where moisture and air infiltrate through them and damage the perovskite film. Therefore, suppressing both the electronic and surface defects are highly required not only to improve the cell performance but also to extend the long-term stability of the PSCs. Various strategies have been investigated to suppress such defects, such as, modifying the perovskite film fabrication techniques (perovskite single crystal), perovskite precursor engineering (doping of perovskite precursor with passivation materials), and post-surface treatment of the perovskite film. The latter strategy is very attractive because the passivation materials are directly deposited on the top surface of the perovskite, as a result, it will hardly alter the underlayer perovskite intrinsic absorption property. Moreover, the post-surface passivation strategy is scalable and could be incorporated into large-area solar modules and panels. Using the ionic nature of perovskite as an opportunity various passivation materials were studied to passivate cation vacancy[5-7] or halide vacancy.[8-15] The halide defects could be passivated by Lewis bases or with similar size anions. The lone pair electrons of the Lewis base-based passivating molecule coordinate with the free orbits of Pb^{2+} ions to passivate the halide vacancies. In a similar fashion, the cation vacancies are passivated with Lewis acid, in which a passivation molecule with free orbital can accept the free electrons from the undercoordinated halides, suppressing cation vacancies. Moreover, equivalent size cations could be directly replaced to treat cation vacancies. The main drawback of Lewis base or Lewis acid passivating agents is they only passivate either the halide defects or cation defects at a time. Therefore, it is necessary to develop zwitterionic-based passivating agents to suppress both the negatively and positively charged defects simultaneously.

Recently, ammonium salt-based passivation molecules demonstrated remarkable improvements in the performance and stability of the PSCs. [16-32] However, there are limited number of studies that demonstrated the passivation of both positively and negatively charged defects concurrently. [33-39] Therefore, it is an urgent need to develop such kind of passivation molecules to eradicate both halide and cation defects simultaneously, boost PCE and extend the long-term stability of the PSCs. Various tetrabutylammonium cation (TBA^+) with different anion derivatives are employed to modify the perovskite defects. Isabella Poli et al. partly substituted MAI with tetrabutylammonium iodide (TBAI) to fabricate 2D $(TBA)_n(MA)_{1-n}PbX_3$ on the surface of 3D perovskite.[17] However, the substituted TBAI negatively influenced the device performance even when the TBAI substituted amount is 1%.[17] Moreover, in their study the role of TBAI anion is not mentioned.[17] Similarly, Shao Jin et al. introduced tetrabutylammonium bromide (TBAB) into the perovskite precursor solution, in which the TBAB tuned the perovskite crystallization as a result high-quality perovskite film achieved, consequently, in this scenario it is hard to understand the sole role of TBAB on passivating the perovskite as it participated in the crystallization process and modified the perovskite morphology.[40] Chaoqun Zhang et al. found that the larger ionic radius PF_6^- (2.55 Å) could substituted I^- (2.20 Å) ions,[41] and the authors expected TP_6 would form a passivation layer on top of the perovskite grains upon the surface passivation using tetrabutylammonium hexafloride. Moreover, in this particular study the new material phase was not investigated.[41] M. Dehghanipou et al. reported passivation of mixed perovskite with tetrabutylammonium tetrafluoroborate ($TBABF_4$), where a 2D/3D perovskite structure formed, however, the best performance of the passivated device is 17.02% and V_{oc} of 0.99V.[42] Tetrabutylammonium chloride (TBACl) was employed to modify $MAPbI_3$, where it was found that the TBACl significantly suppressed iodine vacancies by reducing the I_2 to I_3^-.[43]

Additinally, recent studies demonstrated that the effectiveness of 1D perovskite on the surface modification of the perovskite layer.[44-50] TBA^+-based 1D perovskite was employed to modify various layers of the PSCs. For instance, Xiaomin Liu et.al, showed an interesting study on the interaction of tetrabutylammonium (TBA^+) cation with $CsPbI_3$ to form 1D $TBAPbI_3$.[51] On the other hand, Yuquan Ai et.al presented the successful modification of SnO_2 by tetrabutylammonium fluoride (TBAF), in which an in situ layer of $TBAPbI_3$ perovskitoid at the SnO_2/ $FAPbI_3$ interface.[52] Interestingly, Fluorine-containing molecules demonstrated effective passivation of the perovskite defects, where the strong electronegativity of the Florine promotes the interaction of the molecules with perovskite to suppress the uncoordinated Pb significantly.[53, 54] As a result defects were suppressed and both PCE and long-term stability were improved.

Inspire by the latter two studies, here, we employed TBATFB as a post-surface modifier for the mixed perovskite layer with a composition of $Cs_{0.05}(FA_{0.83}MA_{0.17})_{0.95}Pb(I_{0.83}Br_{0.17})_3$ in short CsFAMA. TBATFB is a symmetrical quaternary ammonium salt with a central cation and surrounded by a tetrafluoroborate anion. The ionic nature of TBATFB is crucial to repress both the negatively and positively defects of the perovskite, where the tetrafluoroborate ion (BF_4^-)

interacted with the uncoordinated Pb^{2+} subsequently the halide defects suppressed. Moreover, the anti-sites defects such as PbI_3^- and $PbBr_3^-$ could interacted with the TBA^+ to generate a low-dimensional $TBAPbI_3$ and $TBAPbBr_3$, respectively, as a result defects further suppressed. Furthermore, the TBATFB interacted with the excess PbI_2 and $PbBr_2$ of the mixed perovskite and formed a 1D perovskitoid of $TBAPbI_{1.66}Br_{0.34}BF_4$ over the 3D perovskite surface. Although it precisely required a wide separate study based on the same perovskite composition to understand the influence of various tetrabutylammonium anions derivatives such as I^-, Br^-, Cl^-, F^- and BF_4^- influences on PCE and stability of the PSCs, the latter anion provides two unique advantages over the halide tetrabutylammonium anions derivatives with respect to the energy level alignment and long-term stability. In general, those tetrabutylammonium derivatives could modify the surface, grain boundaries and electronic defects. Moreover, the tetrabutylammonium derivative anions could regulate the interface energy, either upshifted or downshifted, which plays a significant role in the carrier dynamics, recombination and PCE of the device. The tetrabutylammonium anions derivatives which contain I^- anion[51] and Br^- anion[55] exhibited lowering the valence band of perovskite at the interface, on the contrary, our BF_4^- which is a symmetrical fluorine source anion, and shifted the valance band of perovskite upward at the interface, and established a favorable energy alignment with spiro-OMeTAD compared with the tetrabutylammonium halide anion derivatives. As a result, the hole transport could facilitate when TBATFB is employed to passivate perovskite compared to tetrabutylammonium halide derivatives. Moreover, due to more fluoride in the TBATFB, BF_4^- the modified device demonstrated higher water contact angle compared to the tetrabutylammonium halide anion treated perovskite[43, 52] which suggested TBATFB has a positive effect on the long-term stability of the device. Our experimental results revealed the TBATFB-modified perovskite exhibited suppressed surface and electronic defects as a result the

1D/3D perovskite heterostructure exhibited enhanced photoluminescence, V_{oc} and FF. As a result, TBATFB-modified PSCs demonstrated a champion PCE of 21.68% with almost no PCE loss for devices in air (RH=40-60%) for 720 h. The possible reasons for the improvement are critically analyzed and discussed.

Experimental Section

Materials: All the chemicals and FTO substrate used in this study are obtained from the same supplier with our previous report.[56] TBATFB bought from Sigma-Aldrich. All the chemical used as received.

Device Fabrication: The FTO substrates were cleaned and SnO_2 films were prepared following reported literature procedure.[56] Then the SnO_2 layers were UV-Ozone treated for 5 min and followed by transferring to a nitrogen glove box (O_2 and H_2O are < 0.01 ppm) to spin-coat perovskite, TBATFB, and hole-transporting layers.

The mixed perovskite with a composition of $Cs_{0.05}(FA_{0.83}MA_{0.17})_{0.95}Pb(I_{0.83}Br_{0.17})_3$ is prepared and spin-coated following literature report.[57] Next, various concentrations of TBATFB in 2-propanol were spin coated on CsFAMA at 4000 rpm for 30 s and annealed at a mild temperature of 70 ^oC for 10 min. The optimized TBATFB concentration for the champion cell is 1mM. Finally, the spiro-OMeTAD HTL and Au layer deposited following literature.[57]

XRD film preparation: A layer prepared from equimolar TBATFB/PbI_2 (1:1) in DMF/DMSO (4:1 v/v) to study their interaction. The layer is deposited on glass substrate at 1000 rpm for 10 s and 6000rpm for 20 s followed by 70^{o}C backing for 5min.

Film and device characterizations: Perovskite film and device characterizations for both the control and modified films were characterized by XRD, FT-IR, XPS, SEM, UV-Vis, TAS, PL, TRPL, I-V, EQE, and EIS using the apparatus and conditions described in reference.[43, 58]

Results and discussion

Scheme 1a-e illustrates the interaction between TBATFB and perovskite. Various concentrations of TBATFB in 2-propanol were spin-coated on the perovskite film and baked at 70ºC.

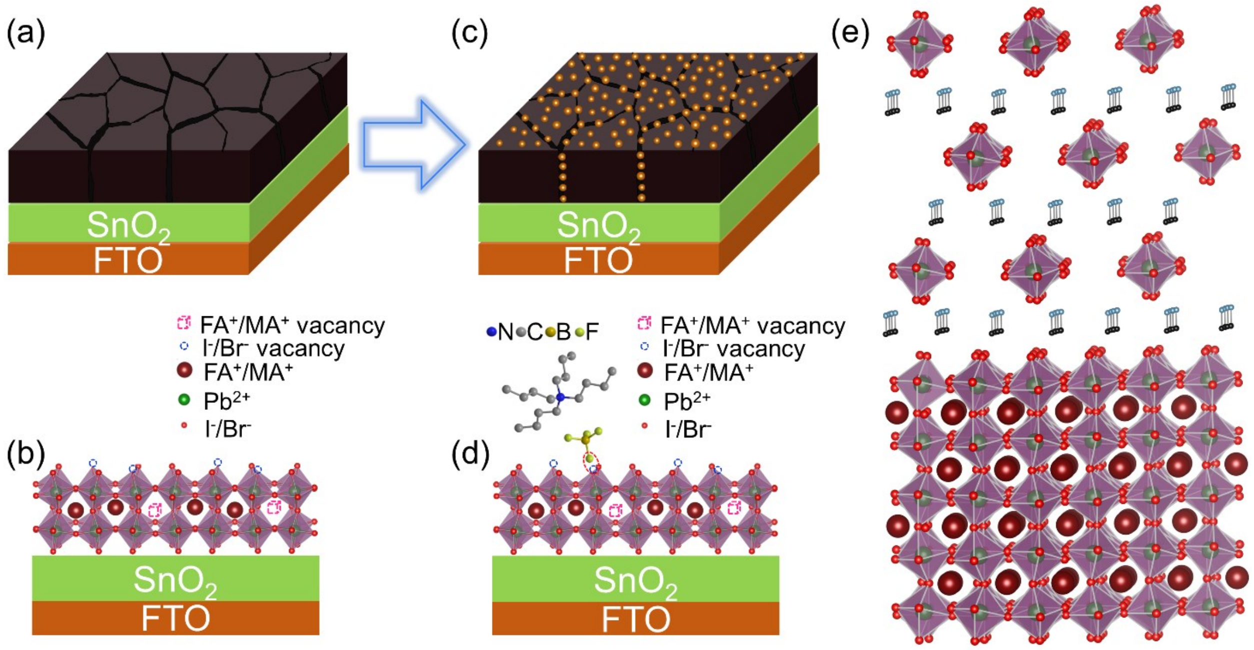

Scheme 1: Schematic illustration of (a) the control perovskite film, (b) TBATFB-modified perovskite film, (c) electronic defects on the control perovskite film, (d) chemical interaction between TBATFB and perovskite, (e) illustration of 1D/3D structure.

To study the chemical interaction between TBATFB and perovskite we carried out FTIR (Figure 1a-d). The control CsFAMA exhibited a sym. N-H stretch at 3265 cm^{-1} and sym. NH_3^+ bend at 1472 cm^{-1} which are shifted to the lower wavenumber of 3258 cm^{-1} and 1470 cm^{-1} for TBATFB-modified perovskite. The asym. C-N stretch at 3399 cm^{-1} of the control perovskite shifted significantly to the lower wavenumber of 3388 cm^{-1} after TBATFB modification. The control sample demonstrated a C-N stretch and CH_3-NH_3^+ rock at 959 cm^{-1} and 905 cm^{-1} which are shifted to the higher wavenumber of 961cm^{-1} and 908 cm^{-1} for the modified CsFAMA. The N-H shift demonstrated the interaction between NH_3^+ of the perovskite and TBATFB through hydrogen bonding. All these shifts are associated with a strong interaction between the perovskite and TBATFB.

To scrutinize the type of interaction we did a series of XRD measurements. As PbI_2 amount in our perovskite composition is significantly higher than $PbBr_2$, first we study the interaction between TBATFB and PbI_2. Equimolar amount of PbI_2 and TBATFB (1:1 molar ratio) were deposited on the glass substrate and XRD was recorded. The XRD peak at ca. 12.6° assigned to the excess PbI_2, intriguingly, there is an emergence of a new peak at about 7.6°, which demonstrated the formation of 1D perovskite (also known as perovskitoid) on the 3D layer following a chemical interaction between PbI_2 and TBATFB.[52] The XRD result is shown in Figure 1e and Figure S1. Considering the above result, we expected TBATFB could interact with the excess PbI_2 and $PbBr_2$ of our mixed perovskite composition to form 1D perovskite capping layer. To confirm this, we measured the XRD of a control perovskite and 1mM TBATFB-modified perovskite. As expected, the XRD of 1mM TBATFB-modified perovskite exhibited an emergence of a new XRD peak at 7.2°, slightly shifted to lower angle compared to the PbI_2 and TBATFB based 1D perovskite 2-theta believed due to the additional $PbBr_2$ in CsFAMA. To confirm further, we employed 20mM TBATFB to modify the perovskite. We have observed that the peak intensity further increased with increasing TBATFB concentration (20 mM). We have taken the XRD of TBATFB on glass, where this organic molecule exhibited a broad peak at about 23°. Therefore, those detail characterization verified that the new emerging peak is formed from the interaction between the excess PbI_2/$PbBr_2$

and TBATFB on the perovskite surface. Interestingly, this peak is signifying the in-situ formation of 1D perovskite of $TBAPbI_{1.66}Br_{0.34}BF_4$ over the 3D perovskite to produce a 1D/3D heterostructure.[51, 52]

Then, we have studied the 2D-GIWAXS of the control and TBATFB-modified perovskite films to reconfirm the formation of a 1D perovskite on the surface of 3D perovskite. The 2D-GIWAXS investigation is presented in Figure 1f-h, where the control perovskite showed a diffraction ring at 1Å, 1.4Å, 1.73Å, 2Å, 2.23Å, 2.45Å, 2.83Å and 3Å corresponding to a 2-theta of 14.1°, 19.83°, 24.48°, 28.36°, 31.76°, 35°, 40.55°, and 43.18° respectively. Intriguingly, the TBATFB-modified perovskite has shown an additional intense diffraction ring at 0.51Å (Figure 1g-h) equivalent to a 2-theta of 7.23° which explicitly confirmed the formation of 1D perovskite which is indexed as the (200) reflection plane of $TBAPbI_{1.66}Br_{0.34}BF_4$.[51] All the FTIR, XRD and 2D-GIWAXS validated the strong interaction between perovskite and TBATFB and the formation of 1D $TBAPbI_{1.66}Br_{0.34}BF_4$ on the surface of the 3D perovskite. This low-dimensional 1D perovskites (perovskitoid) capping layer not only represses the defects in perovskite by blocking the nonradiative recombination centers in the device but also safeguards the 3D perovskite from the infiltration of moisture and deterioration by which the long-term stability of the solar cell extends.

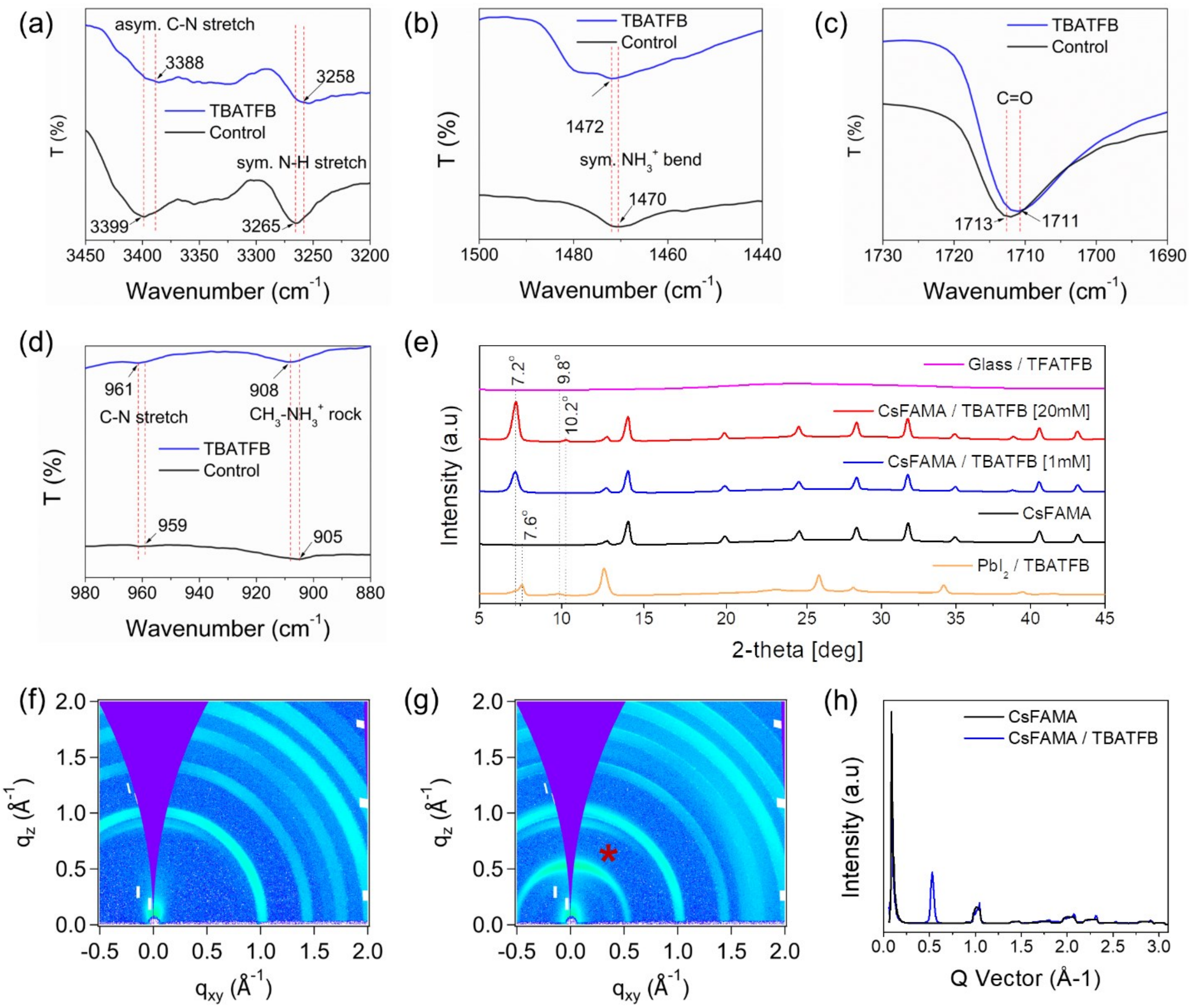

Figure 1: Characterization of the interaction between CsFAMA and TBATFB. (a-d) FTIR spectra of the control and TBATFB-modified perovskite films at various wavenumber regions. (e) XRD of PbI_2 modified TBATFB, control CsFAMA, CsFAMA modified with 1mM TBATFB, CsFAMA modified with high concentration 20mM TBATFB, and TBATFB film on glass. (f) 2D-GIWAXS of the control CsFAMA, (g) 2D-GIWAXS of TBATFB-treated CsFAMA, (h) Q Vector comparison of the control and TBATFB-modified CsFAMA. The * denotes the emerging 1D perovskite.

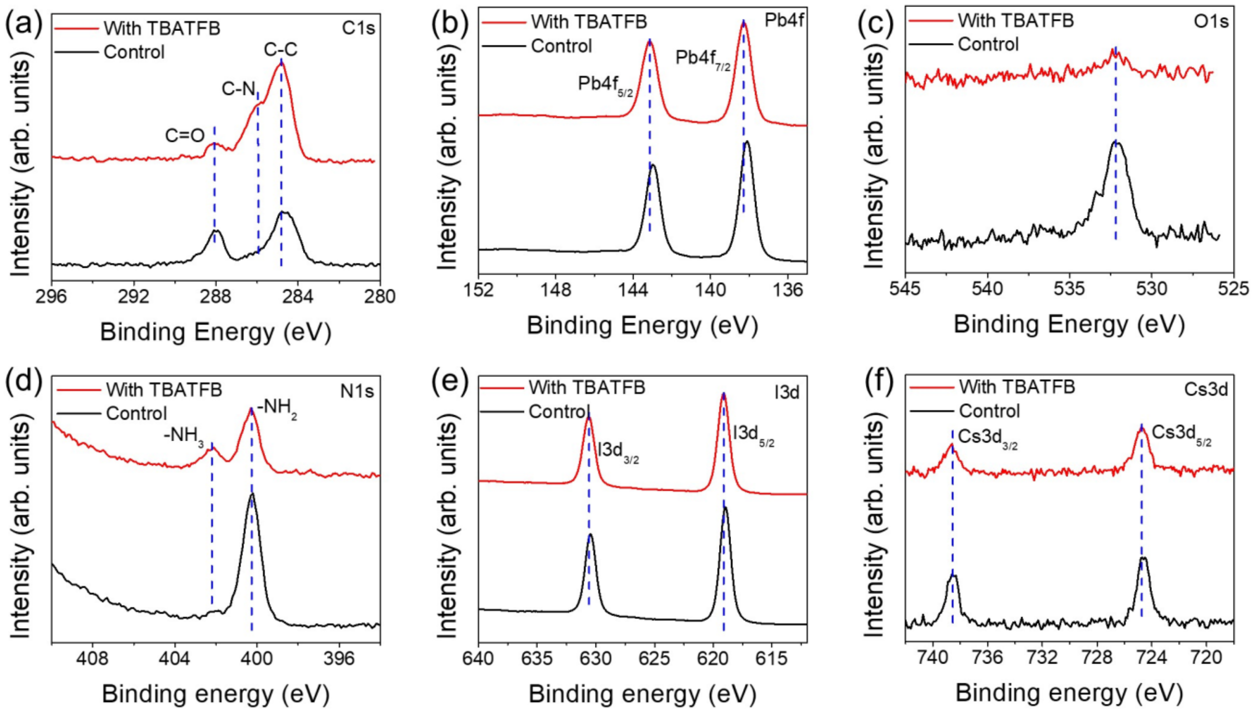

Figure 2: High-resolution XPS spectra of (a) C1s, (b) Pb4f (c) O1s, (d) N1s, (e) I3d and (f) Cs3d for control and TBATFB modified perovskite films.

The chemical composition changes of C1s, N1s, Pb4f, I3d, O1s, Cs3d, and Fls are studied in detail before and after TBATFB modification via x-ray photoelectron spectroscopy (XPS). The C1s spectra are presented in Figure 2a. Initially, the C-C peaks for both the control and TBATFB-modified perovskite films are charge corrected at 284.8 eV.[59] Moreover, a new shoulder peak appeared at 285.94eV after TBATFB modification which is assigned to the C-N bond.[59] The peak at 288.03 eV is assigned to C=O. The F1s spectrum at 687.54 eV (Figure S2) verified the presence of TBATFB on the surface of the perovskite, this spectrum is the signature peak for the modified perovskite because the F1s signal is not present in the control CsFAMA.

The Pb4f spectra is presented in Figure 2b, where the two principal peaks of $Pb4f_{5/2}$ and $Pb4f_{7/2}$ are shown at 142.94 eV and 138.08 eV, respectively for the control perovskite, which are shifted to the higher binding energy of 143.14 eV and 138.28 eV, respectively for the TBATFB-modified perovskite. The shift undoubtedly infers the interaction between [PbX_6^{4-}] and TBATFB, through which the halide vacancies of the perovskite were modified by TBATFB treatment which leads to repressed uncoordinated Pb^{2+} ions.[59] To support this we measured UV-Vis absorption of FAI, TBATFB-modified FAI, PbI_2, TBATFB-modified PbI_2, $PbBr_2$, and TBATFB-modified $PbBr_2$ where we observed the I_3^- and Br_3^- concentration enhanced for the TBATFB-modified solution which clearly indicated that the deep-level halide defects suppressed from the respective films significantly (Figure S4a-c).[43, 60] Expectedly, the C/Pb ratio (intensity ratio of C-C/$Pb4f_{5/2}$) increases from 0.076 to 0.162 with the TBATFB treatment, further confirming the existence of TBATFB on the surface of the perovskite. Fascinatingly, The O/Pb (intensity ratio O1s/$Pb4f_{5/2}$) ratio for the TBATFB-modified perovskite (0.014) also reduced considerably compared to the control O/Pb ratio (0.442) which signifies that the 1D $TBAPbI_{1.66}Br_{0.34}BF_4$ perovskitoid capping layer safeguards the intrusion of moisture and air so that it impedes the perovskite decomposition rather improved the long-term stability of the modified PSCs.

The N1s spectra are presented in Figure 2d, where the control perovskite showed a single peak at 400.20 eV assigned for $-NH_2$, which is shifted to the higher binding energy of 400.29 eV for the TBATFB-modified perovskite.[59] The N1s shift demonstrated the interaction of TBATFB and CsFAMA through hydrogen bonding ($N-H\ldots BF_4^-$).[41, 56, 61] In general, the $[PbX_6]^{4-}$ framework interacted with the A-cation containing ammonium ($-NH_3^+$) groups through hydrogen bonding to form the 3D perovskite structure.[62] Similarly, our bulky-cation TBA^+ could interact with $[PbI_6]^{4-}$ framework on the surface of perovskite through hydrogen bonding.[51] Following, the three-dimensional perovskite structure collapsed, and a one-dimensional chains of face-sharing $[PbI_x]^-$ octahedra on the surface of three-dimensional perovskite emerged.[63]Furthermore, the TBATFB-modified perovskite showed an extra peak at 402.22 eV (assigned to -NH_3) which arises from the TBA^+ cation. These changes clearly demonstrate the interaction between CsFAMA and TBATFB.

Correspondingly, the I3d spectra are shown in Figure 2e, where the two main peaks at 630.41 eV 618.98 eV are assigned to $I3d_{3/2}$ and $I3d_{5/2}$, respectively for the control CsFAMA, which are shifted to the higher binding energy of 630.55 eV and 619.11 eV, respectively for TBATFB-modified CsFAMA. This shift suggested that TBATFB could modify the negatively charged defects such as I^- and Br^-, and anti-sites. The anti-sites such as PbI_3^- and $PbBr_3^-$ could bind with TBA^+ to form another low-dimensional perovskite of $TBAPbI_3$ and $TBAPbBr_3$, respectively, as a result, the anionic defects could further suppressed.[33] Figure 2f shows the Cs3d XPS spectra where the control perovskite exhibited two characteristic peaks at 738.42 eV for $Cs3d_{3/2}$ and 724.57 eV for $Cs3d_{5/2}$ which are shifted to higher binding energy of 738.58 eV and 724.73 eV, respectively for the modified perovskite. All the binding energy shifts associated with the N1s, Pb4f, I3d, and Cs3d and the emergence of Fls for the TBATFB-modified perovskite confirms the interaction of perovskite with TBATFB. Therefore, the XPS results corroborated with the XRD and 2D-GIWAXs where all results verified that the TBATFB has strong interactions with the perovskite and formed a 1D $TBAPbI_{1.66}Br_{0.34}BF_4$ perovskitoid capping layer. We provided the full XPS spectra for CsFAMA and TBATFB-modified CsFAMA in Figure S3.

Following, we drop cast perovskite film from a solution composed of CsFAMA and TBATFB (1:1 molar ratio in DMF) and studied the surface morphology with an optical microscope (Figure S4d), where we found the formation of needle-like structure on top of the 3D perovskite which is a solid evidence for the formation of a new 1D perovskite phase with a composition of $TBAPbI_{1.66}Br_{0.34}BF_4$ following equation 1,[64] which validated our XRD and 2D-GIWAXS. Ref 61 reported that a similar 1D needle like perovskite crystal formed from Lead(II) bromide and N, N’-

dimethylethylenediamine. Ref 40 proposed the substitution of a small amount of I (2.20 Å) ions by PF6 (2.55 Å) ions with a larger ionic radius. These two references support our equation (1). Reference 50 has already provided a sound single crystal X-ray diffraction analysis to prove that the TBAI-PbI$_2$ precursor tends to form a 1D perovskite of TBAPbI$_3$.

$$TBABF_4 + 0.83PbI_2 + 0.17PbBr_2 \rightarrow TBAPbI_{1.66}Br_{0.34}BF_4 \text{ -------------------- eq (1)}^{41, 51}$$

To study the distribution of TBATFB on the perovskite surface and/or grain boundaries we measured top-view and cross-sectional EDS of the control and modified perovskite. The top-view EDS maps for the control and TBATFB-modified surfaces are presented in Figure S5-6, where on the modified film we detected B and F which suggested that the TBATFB is uniformly distributed on the surface of the perovskite. Next, we study the cross-sectional EDS elemental mapping of the control and TBATFB-modified perovskite (Figure S7-8), intriguingly, we have detected the B and F distribution in the modified perovskite cross-section which verified TBATFB could diffuse in the grain boundaries to modify them. Therefore, TBATFB is not only uniformly distributed all over the perovskite surface but also diffuses longitudinally into the polycrystalline grain boundaries of the film to modify both the surface and grain-boundaries of the perovskite layer.

Once we confirmed the interaction between perovskite and TBATFB we have investigated the influence of TBATFB modification on the optical, charge extraction, trap density of states and surface properties. The UV-Vis absorption spectra of the control and TBATFB-modified perovskite were presented in Figure S9, where there is no significant absorption influence by the TBATFB modification compared to the control perovskite. This displayed very thin 1D capping layer formed on the surface of the perovskite. Due to small amount of TBATFB was employed to passivate the perovskite, it is hard to detect the influence of 1D absorption with the UV-Vis instrument.

Next, steady-state photoluminescence (PL) and time-resolved PL of the control and TBATFB-modified perovskite were studied. The PL of the control and modified perovskite were deposited on the glass substrate and the light is guided from the perovskite side. The PL results were presented in Figure 3a, where the modified film exhibited remarkable improvement (two-fold) compared to the control CsFAMA which signifies the trap densities on the surface and grain boundaries of the control perovskite film were significantly suppressed by TBATFB modification. Two defect suppression mechanisms were proposed: the TBATFB interacted with the perovskite layer and modified the electronic defects by which the non-recombination centers significantly repressed, and it can fill the GBs to modify the surface defects. Moreover, TBATFB reacted with the perovskite and formed hydrophobic 1D perovskite capping layer which could protect the perovskite film from degradation and modifying the interface energy for favorable charge extraction. This combined defect treatment results in a superior PL for the modified film.

To understand the details of charge transfer dynamics we measure the TRPL of the control and TBATFB-modified perovskite. The lifetimes are calculated by following equations (1) and (2).

$$\mathrm{Y} = A_1 \exp\left(\frac{-t}{\tau_1}\right) + A_2 \exp\left(\frac{-t}{\tau_2}\right) \qquad \text{equation (1)}$$

$$\tau_{avg} = \frac{A_1 {\tau_1}^2 + A_2 {\tau_2}^2}{A_1 \tau_1 + A_2 \tau_2} \qquad \text{equation (2)}$$

Where A_1 and A_2 are the relative amplitudes, t is time, τ_1 and τ_2 are the lifetime values for the fast and slow decay, respectively.

The average lifetime of the control film was 321.49 ns, and upon TBATFB treatment the perovskite has shown a longer average lifetime of 408.90 ns which implies the reduction of defects in the film with TBATFB treatment. The TRPL is presented in Figure 3b, and the lifetime results are summarized in Table S1.

Afterwards, we fabricated electron-only and hole-only devices to quantify the number of electron and hole defects on the control and TBATFB-modified perovskite devices. The number of defects is calculated using equation 3, where ε is the relative dielectric constant. As $FAPbI_3$ accounted ca.79%v composition of the CsFAMA we took ε of $FAPbI_3$[10, 65](ε=46.9). ε_0 is vacuum permittivity. V_{TFL} is trap-filled limit voltage. e is the elementary charge. L is the thickness of the control and TBATFB-modified perovskite, and N_{traps} is the number of traps.

$$N_{traps} = \frac{2\varepsilon\varepsilon_0 V_{TFL}}{eL^2} \qquad \text{equation (3)}$$

The electron-only devices are fabricated with a structure of FTO/SnO_2/CsFAMA (with and without TBATFB)/PCBM/Au and measured under dark conditions. The double logarithmic graph of the control and TBATFB-modified electron-only devices are presented in Figure 3c-d. The N_{traps} for the control device is $14.53\times10^{15}cm^{-3}$. The TBATFB device N_{traps} significantly reduced to $6.89\times10^{15}cm^{-3}$. Next, the hole-only device with a structure of FTO/PTAA/CsFAMA (with and without TBATFB)/Spiro-OMeTAD/Au is fabricated to quantify hole traps. The control and TBATFB-modified hole-only devices are presented in Figure 3e-f, where the control device showed $7.15\times10^{15}cm^{-3}$ N_{traps}. Upon TBATFB passivation the N_{traps} decreased to $5.68\times10^{15}cm^{-3}$. These revealed the potential of TBATFB to heal both cationic and anionic defects from the perovskite. The N_{traps} study is consistent with the PL study. Full SCLC parameters are summarized in Table S2.

The surface roughness of the control and TBATFB-modified perovskite is characterized by atomic force microscopy and presented in Figure 3g-h and Figure 3i-j, respectively. The surface roughness of the control perovskite is 25.1 nm. We didn't observe significant difference on the surface roughness of the perovskite layer by TBATFB modification. The roughness slightly decreased to 24.1 nm. It is clearly seen that crystal sizes and morphology of the modified surface are different which are closely contacted compared to the control perovskite. To elucidate this, we take the top view SEM images of the control and TBATFB-modified perovskite films. The SEM monograms are presented in Figure 3k-l and Figure S10. On the SEM monogram of the control film, there are a lot of white spots all over the surface which are the excess PbI_2 images. After 1mM TBATFB modification there are no PbI_2 spots and a different morphology formed, which signifies the reaction of excess PbI_2 and TBATFB to form the one-dimensional $TBAPbI_{1.66}Br_{0.34}BF_4$. The SEM result corroborates the XRD and 2-D GIWAXS results.

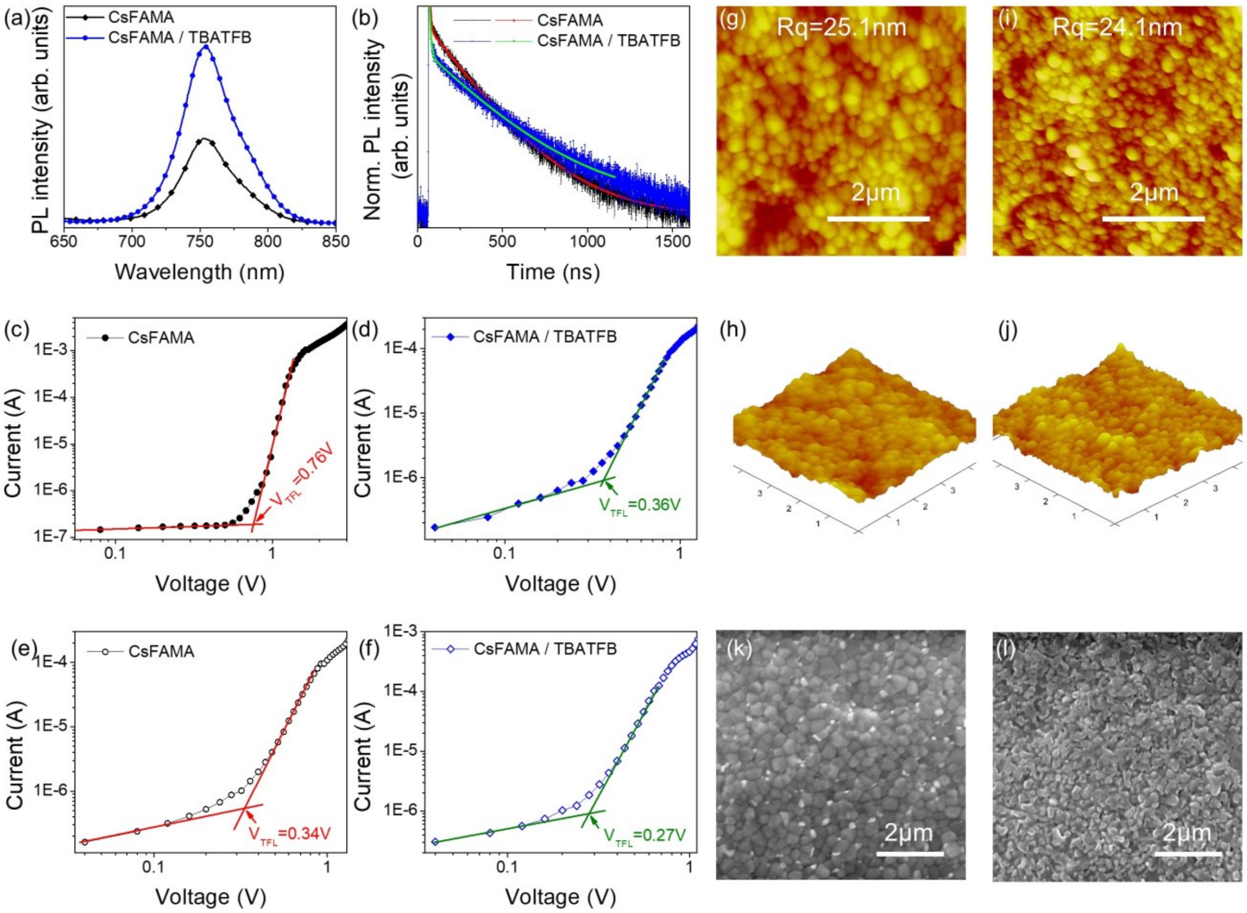

Figure 3: (a) Steady state PL of the control and TBATFB-modified perovskite films. (b) TRPL of the control and TBATFB-modified perovskite films. (c-d) Electron only device with a structure of FTO/SnO_2/CsFAMA (with and without TBATFB)/PCBM/Au, (e-f) Hole only device with a structure of FTO/PTAA/CsFAMA (with and without TBATFB)/Spiro-OMeTAD/Au. AFM surface and 3-dimensional images of the control (g-h) and TBATFB-modified perovskite films respectively (i-j). (k) SEM of the control perovskite, and (l) SEM of TBATFB-modified perovskite.

Femtosecond transient absorption spectroscopy (fs TAS) measurements were performed to further understand and elucidate the effect of TBATFB modification on the charge carrier dynamics and defect passivation. Generally, the carrier trapping in the deep sub-gap state is the primary cause for rapid nonradiative recombination, which limits the quasi-Fermi level splitting and V_{oc} of the PSCs.[66] An increase in the photoluminescence from modified perovskite in comparison to the control perovskite (Figure 3a) could be related to the slow recombination. A femtosecond laser system that comprises a Titanium–Sapphire regenerative amplifier (Astrella, M/s Coherent Inc.) delivering femtosecond pulses of ~100 fs pulse width, a wavelength of 800 nm at 1 kHz repetition rate, an automated transient absorption spectrometer (HELIOS Fire, M/s Ultrafast systems) were used to perform femtosecond transient absorption spectroscopy measurements. Part of the amplifier output (2.4 W) was fed to an optical parametric oscillator system (TOPAS, Coherent Inc.) to generate a tunable pump (280-1100 nm), and a laser power of (< 1 W) was used to generate a probe spanning in the region of 400-800 nm. Both the control and TBATFB-modified perovskite films coated on quartz substrate were excited at 600 nm pump-pulses at two different incident powers of 60 and 100μW corresponding to 3.81 and 6.36 $\mu J/cm^{-2}$. Figure 4a-band Figure S11a-b represent the difference absorption spectra (ΔA) of the control and TBATFB-modified perovskite in the 630-800 nm wavelength range at 60 and 100 μW, respectively.

The TA plots of the control and TBATFB-modified perovskite exhibited the following characteristics: (i) a negative band in the spectral region of 660-780 nm representing the ground state bleach or photo bleach (GSB or PB), (ii) a broad positive spectral band in the 630-705 nm spectral region corresponds to the transitions of newly state-filling excited-state carriers to higher levels., and (iii) a second positive absorption band in the 760 to 780 nm region assigned to a transient Stark effect caused by the Coulomb interactions between the hot-excitons and the band-edge excitons.[67, 68]. A negative peak at ~740 nm is assigned to the PB/GSB of the respective perovskites, where the intensity of GSB increases with time at initial timescales and decreases back to the ground state at longer time delays for both films. Though the magnitude of GSB is smaller in the TBATFB-modified than the control perovskite, the smaller magnitude of GSB replenishing rates (when compared at 1 ps to 1 ns) in the modified-perovskite explicitly demonstrates the long life of charge carriers (Table S3), which suggested the suppression of nonradiative recombination charge carriers in the perovskite film due to the modification.[69] An increase in the bandwidth of GSB with an increase in incident power/fluence (Figure 4a-b Vs Figure S11a-b) suggests that more charge carriers are accumulated at the band edges of the conduction band and valence band.[70] A subtle blue shift in the GSB peak from 743 nm to 738 nm in the control, and 742 nm to 739 nm in modified perovskite was observed upon increasing laser fluences. Further, it should be noted that band in the 760 to 780 nm region quickly decays, within or around 500 fs, even before the maximum bleach is obtained. Subsequently, the decay kinetics of GSB were studied to understand the transient bleach recovery. Figure 4c depicts the kinetic traces of the control and TBATFB-modified GSB obtained at 60μW pump power. The kinetic traces of the control and modified perovskite obtained at 100 μW pump power is shown in Figure S11c. The obtained kinetic fits at both fluences are summarized in Table S4. The kinetic traces decayed bi-exponentially in both films. The short-lived (τ_1) and long-lived (τ_2) lifetime could be related to trap-assisted recombination and carrier radiative recombination timescales, respectively.[68] The average lifetime (τ_{ave}) was obtained according to the equation (eq 2). The overall longer decay times exhibited by the passivated perovskite could be attributed to the suppression of nonradiative recombination after the TBATFB treatment.

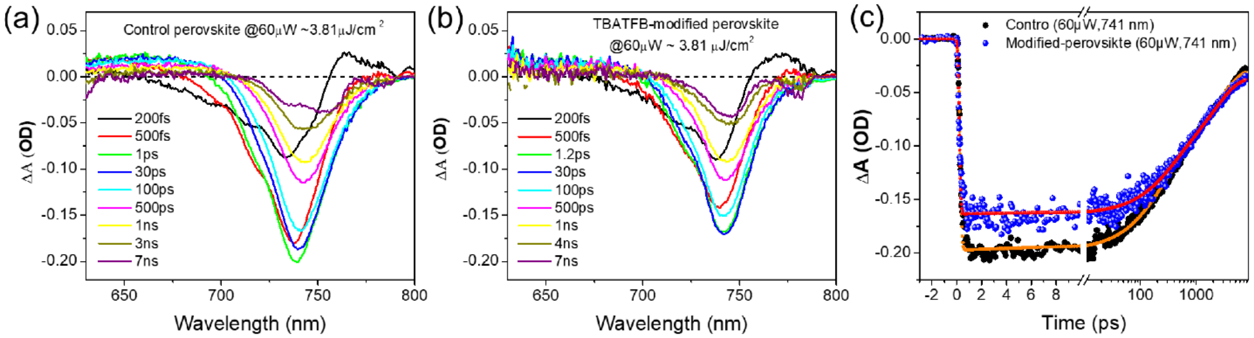

Figure 4: Difference absorption spectra plots of (a) the control, and (b) TBATFB-modified perovskite using laser pulse excitation (600 nm, 3.81 μJ/cm2). (c) GSB decay curves of the control and TBATFB-modified perovskite at (741 nm, 60 μW).

Afterwards, we measured ultraviolet photoelectron spectroscopy (UPS) of the control and TBATFB-modified perovskite to investigate the influence of TBATFB on the energy level. The UPS investigation (Figure S12) demonstrated that the TBATFB-modified perovskite exhibited suitable energy level alignment with the spiro-OMeTAD, leading to facile charge transport and improved device performance.[59]

After that perovskite solar cells with a structure of FTO/SnO_2/CsFAMA (with and without TBATFB)/Spiro-OMeTAD/Au (depicted in Figure 5a) were fabricated to examine the potential of TBATFB modification on the photovoltaic parameters of PSCs. Various concentrations of TBATFB (0mM, 0.5mM, 1mM, 1.5mM, 2mM and 3mM) in 2-propanol were spin coated on the perovskite layer by which the best concentration was optimized. The optimization is summarized in the box chart in Figure S13. The box chart clearly demonstrated a very small amount of TBATFB is sufficient to passivate the electronic defects of the perovskite as a result the V_{oc} and FF of the device incredibly improved with a minimal dose of only 1mM TBATFB treatment. When the concentration increases above 1mM both the V_{oc} and FF decrease. The excess amount of

TBATFB acts as an insulator and induces the charge resistance of the cell as a result the FF decrease.

To check the reproducibility of our process we fabricated 53 devices from a control perovskite and 81 devices with the TBATFB-modified perovskite. The results summarized on the box chart in Figure 5b-e, obviously showed improvement of V_{oc} and FF for TBATFB-modified perovskite which validates the surface modification happened as a result defects were suppressed. Consequently, a champion remarkable performance of 21.68% PCE achieved for TBATFB-modified perovskite with a J_{sc} of 24.35mAcm^{-2}, a V_{oc} of 1.15V, and FF of 77.41% compared to the control device with a champion PCE of 20.03% with a J_{sc} of 23.85mAcm^{-2}, a V_{oc} of 1.12V, and FF of 75.5%. Our device performance is one of the highest reported on tetrabutylammonium derivatives-based anions, particularly with high V_{oc}. For comparison, we summarized the photovoltaic parameters of various tetrabutylammonium derivatives anions in Table S5. V_{oc} of the device is strongly associated with the recombination behavior of the solar device, therefore, we explored the carrier dynamics of the control and TBATFB modified PSCs by analyzing the light intensity dependence of V_{oc} which provides the crucial information on the recombination processes in the PSCs. The ideality factor (n) is calculated as $n= (q/KT) \times (\Delta V_{oc}/\Delta \ln JL)$, where q is the elementary charge, K is the Boltzmann constant, T is absolution temperature, and JL is the photogenerated current density and the result is summarized in Figure S14. The control device exhibited n=1.95, which indicated the dominant recombination in the control device is trap-assisted Shockley–Read–Hall recombination. Intriguingly, the ideality factor decreased to n=1.62 for the TBATFB-passivated device which clearly demonstrated trap-assisted recombination significantly suppressed by TBATFB modification, as a result, the modified device exhibited outstanding V_{oc}. The ideality factor study corroborated with the J-V measurement. The champion device I-V curve is presented in Figure 5f. Different bias PCE of the control and TBATFB-modified device are summarized in Figure 5g-h. The hysteresis of the control and TBATFB-modified devices were calculated and summarized in Table S6, where the TBATFB device demonstrated slightly better hysteresis index (HI=0.02) compared to the control device (HI=0.03). The external quantum efficiency (EQE) of the control and TBATFB-modified devices are presented in Figure 5i. The integrated J_{sc} of 20.91 mAcm^{-2} was measured for the control device and the integrated J_{sc} of 21.65 mAcm^{-2} was measured for the TBATFB-modified device. There is a discrepancy of *Ca.* 11% between the integrated J_{sc} and the J_{sc} measured in the I–V curve. Such inconsistency arises from the different light sources employed for the two measurements. The EQE measurement is carried out in a single wavelength with considerably lower intensity than the one sun radiation.[71] The discrepancy within 20% signifies a reasonable correlation.[72]

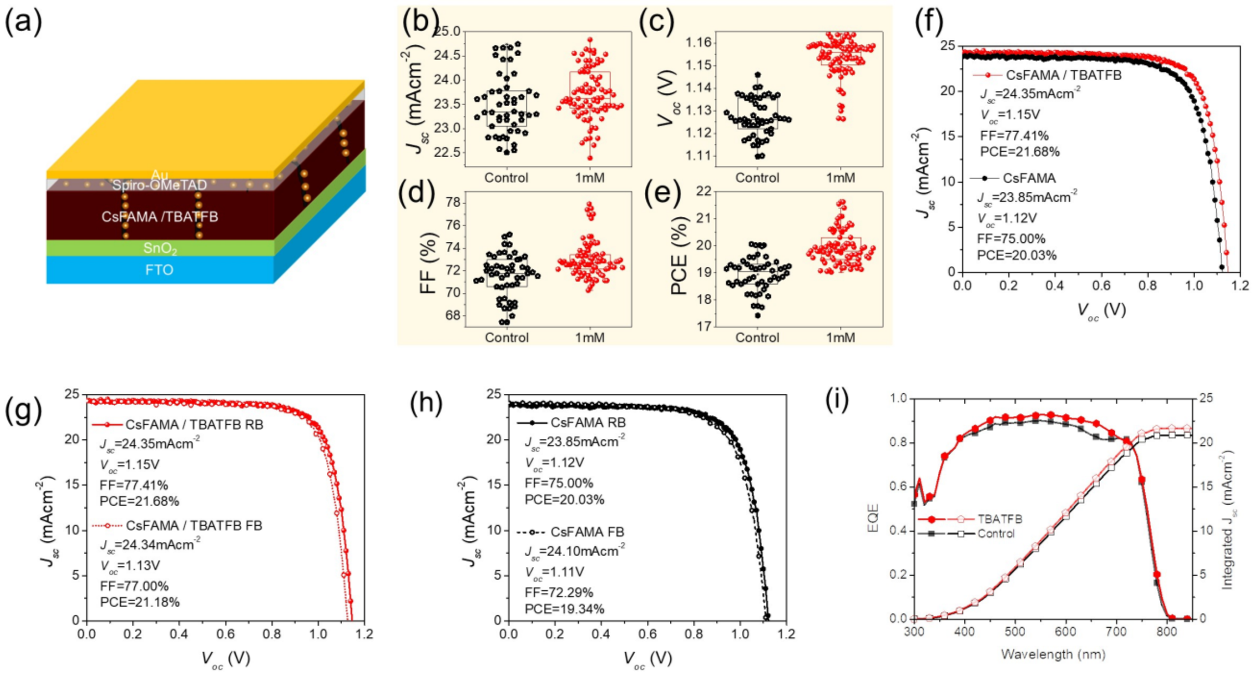

Figure 5. (a) Schematic representation of the fabricated device with a structure of FTO/SnO$_2$/CsFAMA/TBATFB/Spiro-OMeTAD/Au. Box chart comparison of the J-V parameters

for the control and 1mM TBATFB-modified CsFAMA (b) J_{sc}, (c) V_{oc}, (d) FF and (e) PCE. (f) The control and 1mM TBATFB-modified CsFAMA device champion performance. (g) Reverse and forward bias J-V profile of the TBATFB-modified device. (h) Reverse and forward bias J-V profile of the control device. (i) EQE and integrated J_{sc} of the control and TBATFB-modified device.

Next, we investigate the stability of the control and TBATFB-modified perovskite films. The control perovskite showed a water contact angle of 54.79° (Figure 6a). After TBATFB surface treatment the water contact angle increased to 76.85° (Figure 6b), which implies that the formed perovskitoid capping layer not only improved the PL and charge transport besides it could protect the underlying 3D perovskite film by preventing the penetration of moisture. Finally, we studied the long-term stability of the control and TBATFB-modified perovskite devices. The devices were stored in air at room temperature and RH of 40-60% for 720 h. Four unencapsulated devices for each of the control and TBATFB devices were investigated to ensure the long-term study is reproducible. Interestingly, devices fabricated with the TBATFB-modified perovskite exhibited phenomenal stability in which devices retained more than 99% of their initial performance. In contrast, the control device only maintained 82.6% of the initial performance. This demonstrated that TBATFB not only improved the device performance as well it extended the long-term stability of the PSCs. The long-term stability of the control and TBATFB devices is shown in Figure 6c-f. Moreover, we analyzed the thermal stability of the control and TBATFB-modified unencapsulated devices, where the cells were heated at 85°C in the dry air glove box (RH=15±5). It is clearly seen that the control device degraded in a short time. However, the TBATFB-treated device lost PCE initially, but it maintained above 70% of its initial performance which is promising proof of concept to design better passivation molecules to improve the thermal stability of PSCs. The graph is provided in Figure S15.

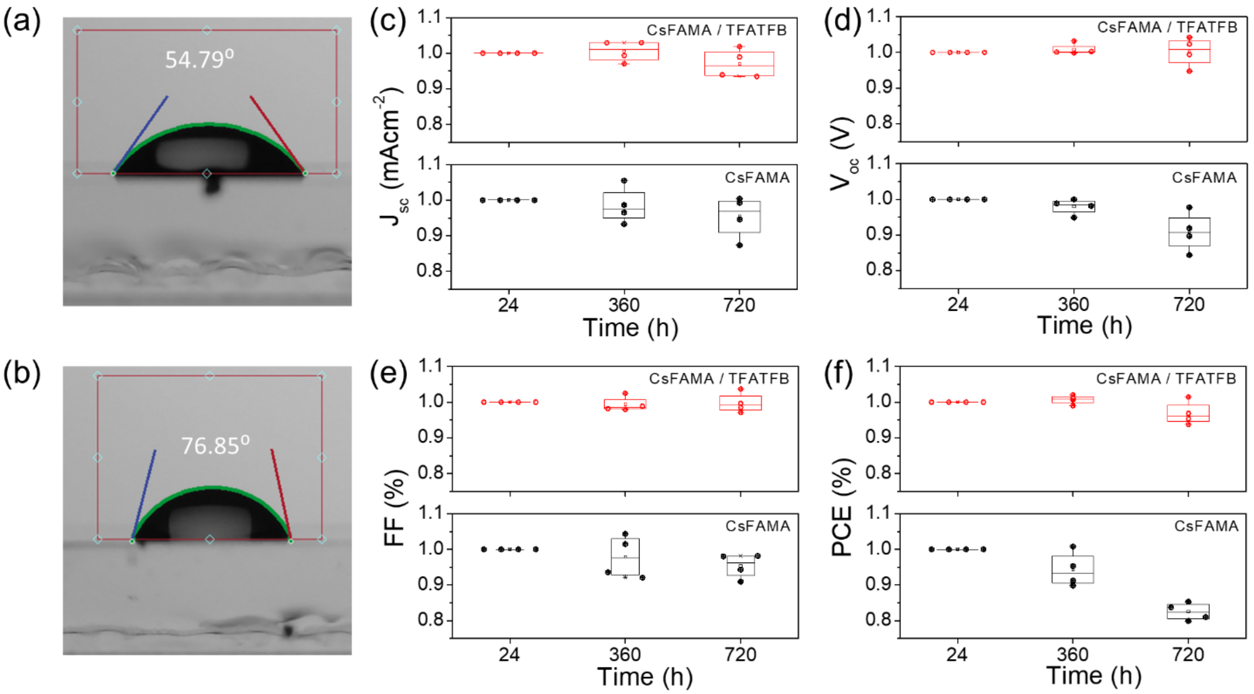

Figure 6. Water contact angle of (a) control perovskite, and (b) TBATFB-modified perovskite layer. Long-term stability of the control and 2mM TBATFB-modified device in air (RH= 40-60%) for 720 hours (c) J_{sc}, (d) V_{oc}, (e) FF and (f) PCE.

Conclusion

In summary, we have effectively treated the surface of the commonly fabricated $Cs_{0.05}(FA_{0.83}MA_{0.17})_{0.95}Pb(I_{0.83}Br_{0.17})_3$ with a TBATFB. By employing a series of characterization techniques including FTIR, XRD, 2D-GIWAXs, XPS, fs TAS, and UV-Vis we revealed the role of TBATFB on perovskite passivation. TFB^- interacted with the $[PbX_6^{4-}]$ framework to suppress the halide vacancies as a result the uncoordinated Pb^{2+} ions suppressed effectively. In the meantime, the bulky TBA^+, which couldn't incorporate into the 3D structure, interacted with anti-site defects such as PbI_3^- and $PbBr_3^-$ and modified the cation vacancies. As a result, TBATFB effectively modify both positively and negatively charged defects. These results are corroborated with the

SCLC investigation, in which, both the electron and hole traps suppressed by TBATFB modification. Furthermore, TBATFB reacted with the excess PbI_2/ $PbBr_2$ and formed a one-dimensional perovskitoid of $TBAPbI_{1.66}Br_{0.34}BF_4$. The perovskitoid-modified perovskite exhibited a significant improvement in the PL, V_{oc}, and FF due to the suppressed surface and electronic defects. Consequently, the 1D/3D heterostructure-based device demonstrated a champion PCE of 21.68%. Additionally, the TBATFB-treatment not only improves the performance of the cells but also extends the stability of perovskite solar cells. Remarkably, TBATFB passivated devices do not show any sign of degradation after 720 h in the air.

Associated Content

Supporting Information

Data including XRD, XPS, UV-vis, EDS elemental mapping and summarized table provided.

Notes

The authors declare no competing financial interest.

Acknowledgment

This material is based on work supported by the National Science Foundation (NSF) under Grant No. 1757220. The steady-state PL and TRPL equipment used in this work is supported by National Science Foundation Research Initiation Award: Novel Perovskite Solar Cells Based on Interface Manipulation (Award#1900047). Q. Dai thanks the support of NSF-PREM grant #DMR-1826886 for the AFM measurements by N. Pradhan. XPS instrumentation used in this work was supported by the NSF Major Research Instrumentation Program (DMR-1726901). Jada Emodogo is supported by the National Science Foundation under Grant No. OIA-2225852.

References

1. Park, J.; Kim, J.; Yun, H. S.; Paik, M. J.; Noh, E.; Mun, H. J.; Kim, M. G.; Shin, T. J.; Seok, S. I. Controlled Growth of Perovskite Layers with Volatile Alkylammonium Chlorides. *Nature* **2023,** *616*, 724-730.
2. Min, H.; Lee, D. Y.; Kim, J.; Kim, G.; Lee, K. S.; Kim, J.; Paik, M. J.; Kim, Y. K.; Kim, K. S.; Kim, M. G.; Shin, T. J.; Il Seok, S. Perovskite Solar Cells with Atomically Coherent Interlayers on SnO_2 Electrodes. *Nature* **2021,** *598*, 444-450.
3. Svane, K. L.; Forse, A. C.; Grey, C. P.; Kieslich, G.; Cheetham, A. K.; Walsh, A.; Butler, K. T. How Strong Is the Hydrogen Bond in Hybrid Perovskites? *J. Phys. Chem. Lett.* **2017,** *8*, 6154-6159.
4. Byranvand, M. M.; Saliba, M. Defect Passivation of Perovskite Films for Highly Efficient and Stable Solar Cells. *Sol. RRL* **2021,** *5*, 2100295
5. Shao, Y.; Xiao, Z.; Bi, C.; Yuan, Y.; Huang, J. Origin and Elimination of Photocurrent Hysteresis by Fullerene Passivation in $CH_3NH_3PbI_3$ Planar Heterojunction Solar Cells. *Nat. Commun.* **2014,** *5*, 5784.
6. Lin, Y.; Bai, Y.; Fang, Y.; Chen, Z.; Yang, S.; Zheng, X.; Tang, S.; Liu, Y.; Zhao, J.; Huang, J. Enhanced Thermal Stability in Perovskite Solar Cells by Assembling 2D/3D Stacking Structures. *J. Phys. Chem. Lett.* **2018,** *9*, 654-658.
7. Jung, E. H.; Jeon, N. J.; Park, E. Y.; Moon, C. S.; Shin, T. J.; Yang, T. Y.; Noh, J. H.; Seo, J. Efficient, Stable and Scalable Perovskite Solar Cells using Poly(3-hexylthiophene). *Nature* **2019,** *567*, 511-515.
8. Jiang, Q.; Zhao, Y.; Zhang, X.; Yang, X.; Chen, Y.; Chu, Z.; Ye, Q.; Li, X.; Yin, Z.; You, J. Surface Passivation of Perovskite Film for Efficient Solar Cells. *Nat. Photonics* **2019,** *13*, 460-466.

9. Son, D. Y.; Kim, S. G.; Seo, J. Y.; Lee, S. H.; Shin, H.; Lee, D.; Park, N. G. Universal Approach Toward Hysteresis-Free Perovskite Solar Cell via Defect Engineering. *J. Am. Chem. Soc.* **2018,** *140*, 1358-1364.

10. Poorkazem, K.; Kelly, Timothy L. Improving the Stability and Decreasing the Trap State Density of Mixed-Cation Perovskite Solar Cells through Compositional Engineering. *Sustain. Energy Fuels* **2018,** *2*, 1332-1341.

11. Zhao, T.; Chueh, C.-C.; Chen, Q.; Rajagopal, A.; Jen, A. K. Y. Defect Passivation of Organic–Inorganic Hybrid Perovskites by Diammonium Iodide toward High-Performance Photovoltaic Devices. *ACS Energy Lett.* **2016,** *1*, 757-763.

12. Uribe, J. I.; Ciro, J.; Montoya, J. F.; Osorio, J.; Jaramillo, F. Enhancement of Morphological and Optoelectronic Properties of Perovskite Films by CH_3NH_3Cl Treatment for Efficient Solar Minimodules. *ACS Appl. Energy Mater.* **2018,** *1*, 1047-1052.

13. Zheng, X.; Yuan, S.; Liu, J.; Yin, J.; Yuan, F.; Shen, W.-S.; Yao, K.; Wei, M.; Zhou, C.; Song, K.; Zhang, B.-B.; Lin, Y.; Hedhili, M. N.; Wehbe, N.; Han, Y.; Sun, H.-T.; Lu, Z.-H.; Anthopoulos, T. D.; Mohammed, O. F.; Sargent, E. H.; Liao, L.-S.; Bakr, O. M. Chlorine Vacancy Passivation in Mixed Halide Perovskite Quantum Dots by Organic Pseudohalides Enables Efficient Rec. 2020 Blue Light-Emitting Diodes. *ACS Energy Lett.* **2020,** *5*, 793-798.

14. Li, Y.; Wu, H.; Qi, W.; Zhou, X.; Li, J.; Cheng, J.; Zhao, Y.; Li, Y.; Zhang, X. Passivation of Defects in Perovskite Solar Cell: From a Chemistry Point of View. *Nano Energy* **2020,** *77*, 105237.

15. Liu, W.; Xiong, J.; Liu, N.; Dai, J.; Dai, Z.; Huang, Y.; Zhang, Z.; Xue, X.; Dai, Q.; Zhang, J. Defect Passivation and Interface Modification by Tetra-n-octadecyl Ammonium Bromide for Efficient and Stable Inverted Perovskite Solar Cells. *Chem. Eng. J.* **2022,** *429*, 132426.

16. Son, D.-Y.; Lee, J.-W.; Choi, Y. J.; Jang, I.-H.; Lee, S.; Yoo, P. J.; Shin, H.; Ahn, N.; Choi, M.; Kim, D.; Park, N.-G. Self-Formed Grain Boundary Healing Layer for Highly Efficient $CH_3NH_3PbI_3$ Perovskite Solar Cells. *Nat. Energy* **2016,** *1*, 16081.

17. Poli, I.; Eslava, S.; Cameron, P. Tetrabutylammonium Cations for Moisture-Resistant and Semitransparent Perovskite Solar Cells. *J. Mater. Chem. A* **2017,** *5*, 22325-22333.

18. Liu, Y.; Akin, S.; Pan, L.; Uchida, R.; Arora, N.; Milić, J. V.; Hinderhofer, A.; Schreiber, F.; Uhl, A. R.; Zakeeruddin, S. M.; Hagfeldt, A.; Dar, M. I.; Grätzel, M. Ultrahydrophobic 3D/2D Fluoroarene Bilayer-Based Water-Resistant Perovskite Solar Cells with Efficiencies Exceeding 22%. *Sci. Adv.* **2019,** *5*, eaaw2543.

19. Stoddard, R. J.; Rajagopal, A.; Palmer, R. L.; Braly, I. L.; Jen, A. K. Y.; Hillhouse, H. W. Enhancing Defect Tolerance and Phase Stability of High-Bandgap Perovskites via Guanidinium Alloying. *ACS Energy Lett.* **2018,** *3*, 1261-1268.

20. De Marco, N.; Zhou, H.; Chen, Q.; Sun, P.; Liu, Z.; Meng, L.; Yao, E. P.; Liu, Y.; Schiffer, A.; Yang, Y. Guanidinium: A Route to Enhanced Carrier Lifetime and Open-Circuit Voltage in Hybrid Perovskite Solar Cells. *Nano Lett.* **2016,** *16*, 1009-16.

21. Hawash, Z.; Raga, S. R.; Son, D. Y.; Ono, L. K.; Park, N. G.; Qi, Y. Interfacial Modification of Perovskite Solar Cells Using an Ultrathin MAI Layer Leads to Enhanced Energy Level Alignment, Efficiencies, and Reproducibility. *J. Phys. Chem. Lett.* **2017,** *8*, 3947-3953.

22. Kubicki, D. J.; Prochowicz, D.; Hofstetter, A.; Saski, M.; Yadav, P.; Bi, D.; Pellet, N.; Lewinski, J.; Zakeeruddin, S. M.; Gratzel, M.; Emsley, L. Formation of Stable Mixed Guanidinium-Methylammonium Phases with Exceptionally Long Carrier Lifetimes for High-Efficiency Lead Iodide-Based Perovskite Photovoltaics. *J. Am. Chem. Soc.* **2018,** *140*, 3345-3351.

23. Alharbi, E. A.; Alyamani, A. Y.; Kubicki, D. J.; Uhl, A. R.; Walder, B. J.; Alanazi, A. Q.; Luo, J.; Burgos-Caminal, A.; Albadri, A.; Albrithen, H.; Alotaibi, M. H.; Moser, J. E.; Zakeeruddin, S. M.; Giordano, F.; Emsley, L.; Gratzel, M. Atomic-Level Passivation Mechanism of Ammonium Salts Enabling Highly Efficient Perovskite Solar Cells. *Nat. Commun.* **2019,** *10*, 3008.

24. Jiang, X.; Chen, S.; Li, Y.; Zhang, L.; Shen, N.; Zhang, G.; Du, J.; Fu, N.; Xu, B. Direct Surface Passivation of Perovskite Film by 4-Fluorophenethylammonium Iodide Toward Stable and Efficient Perovskite Solar Cells. *ACS Appl. Mater. Interfaces* **2021,** *13*, 2558-2565.

25. Wang, Y.; Xu, H.; Wang, F.; Liu, D.; Chen, H.; Zheng, H.; Ji, L.; Zhang, P.; Zhang, T.; Chen, Z. D.; Wu, J.; Chen, L.; Li, S. Unveiling the Guest Effect of N-butylammonium Iodide Towards Efficient and Stable 2D-3D Perovskite Solar Cells Through Sequential Deposition Process. *Chem. Eng. J.* **2020,** *391*, 123589.

26. Yang, B.; Suo, J.; Di Giacomo, F.; Olthof, S.; Bogachuk, D.; Kim, Y.; Sun, X.; Wagner, L.; Fu, F.; Zakeeruddin, S. M.; Hinsch, A.; Gratzel, M.; Di Carlo, A.; Hagfeldt, A. Interfacial Passivation Engineering of Perovskite Solar Cells with Fill Factor over 82% and Outstanding Operational Stability on n-i-p Architecture. *ACS Energy Lett.* **2021,** *6*, 3916-3923.

27. Yang, B.; Suo, J.; Mosconi, E.; Ricciarelli, D.; Tress, W.; De Angelis, F.; Kim, H.-S.; Hagfeldt, A. Outstanding Passivation Effect by a Mixed-Salt Interlayer with Internal Interactions in Perovskite Solar Cells. *ACS Energy Lett.* **2020,** *5*, 3159-3167.

28. Zhuang, J.; Mao, P.; Luan, Y.; Yi, X.; Tu, Z.; Zhang, Y.; Yi, Y.; Wei, Y.; Chen, N.; Lin, T.; Wang, F.; Li, C.; Wang, J. Interfacial Passivation for Perovskite Solar Cells: The Effects of the Functional Group in Phenethylammonium Iodide. *ACS Energy Lett.* **2019,** *4*, 2913-2921.

29. Hauschild, D.; Seitz, L.; Gharibzadeh, S.; Steininger, R.; Jiang, N.; Yang, W.; Paetzold, U. W.; Heske, C.; Weinhardt, L. Impact of n-Butylammonium Bromide on the Chemical and Electronic Structure of Double-Cation Perovskite Thin Films. *ACS Appl. Mater. Interfaces* **2021**, 53202−53210.

30. Krishna, A.; Akhavan Kazemi, M. A.; Sliwa, M.; Reddy, G. N. M.; Delevoye, L.; Lafon, O.; Felten, A.; Do, M. T.; Gottis, S.; Sauvage, F. Defect Passivation via the Incorporation of Tetrapropylammonium Cation Leading to Stability Enhancement in Lead Halide Perovskite. *Adv. Funct. Mater.* **2020,** *30*, 1909737.

31. Mohd Yusoff, A. R. b.; Vasilopoulou, M.; Georgiadou, D. G.; Palilis, L. C.; Abate, A.; Nazeeruddin, M. K. Passivation and Process Engineering Approaches of Halide Perovskite Films for High Efficiency and Stability Perovskite Solar Cells. *Energy Environ. Sci.* **2021,** *14*, 2906-2953.

32. Xiong, J.; Dai, Z.; Zhan, S.; Zhang, X.; Xue, X.; Liu, W.; Zhang, Z.; Huang, Y.; Dai, Q.; Zhang, J. Multifunctional Passivation Strategy Based on Tetraoctylammonium Bromide for Efficient Inverted Perovskite Solar Cells. *Nano Energy* **2021,** *84*, 105882.

33. Zheng, X.; Chen, B.; Dai, J.; Fang, Y.; Bai, Y.; Lin, Y.; Wei, H.; Zeng, Xiao C.; Huang, J. Defect Passivation in Hybrid Perovskite Solar Cells using Quaternary Ammonium Halide Anions and Cations. *Nat. Energy* **2017,** *2*, 17102.

34. Zhang, T.; Xie, L.; Chen, L.; Guo, N.; Li, G.; Tian, Z.; Mao, B.; Zhao, Y. In Situ Fabrication of Highly Luminescent Bifunctional Amino Acid Crosslinked 2D/3D $NH_3C_4H_9COO(CH_3NH_3PbBr_3)_n$ Perovskite Films. *Adv. Funct. Mater.* **2017,** *27*, 1603568.

35. Ye, S.; Rao, H.; Zhao, Z.; Zhang, L.; Bao, H.; Sun, W.; Li, Y.; Gu, F.; Wang, J.; Liu, Z.; Bian, Z.; Huang, C. A Breakthrough Efficiency of 19.9% Obtained in Inverted Perovskite Solar Cells by using an Efficient Trap State Passivator Cu(thiourea)I. *J. Am. Chem. Soc.* **2017,** *139*, 7504-7512.

36. Li, X.; Dar, M. I.; Yi, C.; Luo, J.; Tschumi, M.; Zakeeruddin, S. M.; Nazeeruddin, M. K.; Han, H.; Gratzel, M. Improved Performance and Stability of Perovskite Solar Cells by Crystal Crosslinking with Alkylphosphonic Acid Omega-Ammonium Chlorides. *Nat. Chem.* **2015,** *7*, 703-711.

37. Kyoungwon, C.; Junwoo, L.; Hong Il, K.; Cheol Woong, P.; Guan-Woo, K.; Hyuntae, C.; Sungjin, P.; Sang Ah, P.; Taiho, P. Thermally Stable, Planar Hybrid Perovskite Solar Cells with High Efficiency. *Energy Environ. Sci.* **2018,** *11*, 3238-3247.

38. Yang, S.; Dai, J.; Yu, Z.; Shao, Y.; Zhou, Y.; Xiao, X.; Zeng, X. C.; Huang, J. Tailoring Passivation Molecular Structures for Extremely Small Open-Circuit Voltage Loss in Perovskite Solar Cells. *J. Am. Chem. Soc.* **2019,** *141*, 5781-5787.

39. Zhou, X.; Hu, M.; Liu, C.; Zhang, L.; Zhong, X.; Li, X.; Tian, Y.; Cheng, C.; Xu, B. Synergistic Effects of Multiple Functional Ionic Liquid-Treated PEDOT:PSS and Less-Ion-Defects S-Acetylthiocholine Chloride-Passivated Perovskite Surface Enabling Stable and Hysteresis-Free Inverted Perovskite Solar Cells with Conversion Efficiency Over 20%. *Nano Energy* **2019,** *63*, 103866.

40. Jin, S.; Wei, Y.; Rong, B.; Fang, Y.; Zhao, Y.; Guo, Q.; Huang, Y.; Fan, L.; Wu, J. Improving Perovskite Solar Cells Photovoltaic Performance Using Tetrabutylammonium Salt as Additive. *J. Power Sources* **2020,** *450*, 227623.

41. Zhang, C.; Ren, X.; He, X.; Zhang, Y.; Liu, Y.; Feng, J.; Gao, F.; Yuan, N.; Ding, J.; Liu, S. Post-Treatment by an Ionic Tetrabutylammonium Hexafluorophosphate for Improved Efficiency and Stability of Perovskite Solar Cells. *J. Energy Chem.* **2022,** *64*, 8-15.

42. Dehghanipour, M.; Behjat, A.; Amrollahi Bioki, H. Fabrication of Stable and Efficient 2D/3D Perovskite Solar Cells Through Post-Treatment with $TBABF_4$. *J. Mater. Chem. C* **2021,** *9*, 957-966.

43. Qi, Y.; Green, K. A.; Ma, G.; Jha, S.; Gollinger, K.; Wang, C.; Gu, X.; Patton, D.; Morgan, S. E.; Dai, Q. Passivation of Iodine Vacancies of Perovskite Films by Reducing Iodine to Triiodide Anions for High-Performance Photovoltaics. *Chem. Eng. J.* **2022,** *438*, 135647.

44. Chen, Q.; Deng, K.; Shen, Y.; Li, L. Stable One Dimensional (1D)/Three Dimensional (3D) Perovskite Solar Cell with an Efficiency Exceeding 23%. *InfoMat.* **2022,** *4*, e12303.

45. Freestone, B. G.; Smith, J. A.; Piana, G.; Kilbride, R. C.; Parnell, A. J.; Sortino, L.; Coles, D. M.; Ball, O. B.; Martsinovich, N.; Thompson, C. J.; Alanazi, T. I.; Game, O. S.; Tartakovskii, A. I.; Lagoudakis, P.; Lidzey, D. G. Low-Dimensional Emissive States in Non-Stoichiometric Methylammonium Lead Halide Perovskites. *J. Mater. Chem. A* **2019,** *7*, 11104-11116.

46. Kaneko, R.; Kanda, H.; Shibayama, N.; Sugawa, K.; Otsuki, J.; Islam, A.; Nazeeruddin, M. K. Gradient 1D/3D Perovskite Bilayer Using 4 - tert - Butylpyridinium Cation for Efficient and Stable Perovskite Solar Cells. *Sol. RRL* **2021,** *5*, 2000791.

47. Kong, T.; Xie, H.; Zhang, Y.; Song, J.; Li, Y.; Lim, E. L.; Hagfeldt, A.; Bi, D. Perovskitoid-Templated Formation of a 1D@3D Perovskite Structure toward Highly Efficient and Stable Perovskite Solar Cells. *Adv. Energy Mater.* **2021,** *11*, 2101018.

48. Li, L.; Lv, Y.; Liu, Q.; Fan, Z.; Yuan, R.; Tang, W.; Liu, X.; Zhang, P.; Zhang, W.-H. Efficient MA-Free Perovskite Solar Cells with Balanced Carrier Transport Achieved by 4-Trifluorophenylammonium Iodide. *J. Mater. Chem. A* **2022,** *10*, 9161-9170.

49. Yu, S.; Liu, H.; Wang, S.; Zhu, H.; Dong, X.; Li, X. Hydrazinium Cation Mixed $FAPbI_3$-based Perovskite with 1D/3D Hybrid Dimension Structure for Efficient and Stable Solar Cells. *Chem. Eng. J.* **2021,** *403*, 125724.

50. Zhang, H.; Shi, Z.; Hu, L.; Tang, Y. Y.; Qin, Z.; Liao, W. Q.; Wang, Z. S.; Qin, J.; Li, X.; Wang, H.; Gusain, M.; Liu, F.; Pan, Y.; Xu, M.; Wang, J.; Liu, R.; Zhang, C.; Xiong, R. G.; Sha, W. E. I.; Zhan, Y. Highly Efficient 1D/3D Ferroelectric Perovskite Solar Cell. *Adv. Funct. Mater.* **2021,** *31*, 2100205.

51. Liu, X.; Wang, X.; Zhang, T.; Miao, Y.; Qin, Z.; Chen, Y.; Zhao, Y. Organic Tetrabutylammonium Cation Intercalation to Heal Inorganic $CsPbI_3$ Perovskite. *Angew. Chem. Int. Ed.* **2021,** *60*, 12351-12355.

52. Ai, Y.; Zhang, Y.; Song, J.; Kong, T.; Li, Y.; Xie, H.; Bi, D. In Situ Perovskitoid Engineering at SnO_2 Interface Toward Highly Efficient and Stable Formamidinium Lead Triiodide Perovskite Solar Cells. *J. Phys. Chem. Lett.* **2021,** *12*, 10567-10573.

53. Liu, C.; Liu, S.; Wang, Y.; Chu, Y.; Yang, K.; Wang, X.; Gao, C.; Wang, Q.; Du, J.; Li, S.; Hu, Y.; Rong, Y.; Guo, L.; Mei, A.; Han, H. Improving the Performance of Perovskite Solar Cells via a Novel Additive of N,1-Fluoroformamidinium Iodide with Electron-Withdrawing Fluorine Group. *Adv. Funct. Mater.* **2021,** *31*, 2010603.

54. Su, H.; Zhang, J.; Hu, Y.; Du, X.; Yang, Y.; You, J.; Gao, L.; Liu, S. Fluoroethylamine Engineering for Effective Passivation to Attain 23.4% Efficiency Perovskite Solar Cells with Superior Stability. *Adv. Energy Mater.* **2021,** *11*, 2101454.

55. Mi, J.; Chen, Y.; Liu, X.; Wang, X.; Miao, Y.; Qi, Y.; Zhao, Y. Synergistic Stabilization of $CsPbI_3$ Inorganic Perovskite via 1D Capping and Secondary Growth. *J. Energy Chem.* **2022,** *68*, 387-392.

56. Abate, S. Y.; Zhang, Q.; Qi, Y.; Nash, J.; Gollinger, K.; Zhu, X.; Han, F.; Pradhan, N.; Dai, Q. Universal Surface Passivation of Organic-Inorganic Halide Perovskite Films by Tetraoctylammonium Chloride for High-Performance and Stable Perovskite Solar Cells. . *ACS Appl. Mater. Interfaces* **2022,** *14*, 28044-28059.

57. Abate, S. Y.; Jha, S.; Ma, G.; Nash, J.; Pradhan, N.; Gu, X.; Patton, D.; Dai, Q. Surface Capping Layer Prepared from the Bulky Tetradodecylammonium Bromide as an Efficient Perovskite Passivation Layer for High-Performance Perovskite Solar Cells. *ACS Appl. Mater. Interfaces* **2022,** *14*, 56900−56909.

58. Abate, S. Y.; Yang, Z.; Jha, S.; Ma, G.; Ouyang, Z.; Zhang, H.; Muhammad, S.; Pradhan, N.; Gu, X.; Patton, D.; Wang, K.; Li, D.; Cai, J.; Dai, Q. Room Temperature Slot-Die Coated Perovskite Layer Modified with Sulfonyl-γ-AApeptide for High Performance Perovskite Solar Devices. *Chem. Eng. J.* **2023,** *457*, 141199.

59. Wang, S.; Cao, F.; Wu, Y.; Zhang, X.; Zou, J.; Lan, Z.; Sun, W.; Wu, J.; Gao, P. Multifunctional 2D Perovskite Capping Layer using Cyclohexylmethylammonium Bromide for Highly Efficient and Stable Perovskite Solar Cells. *Mater. Today Phys.* **2021,** *21*, 100543.

60. Yang, W. S.; Park, B.-W.; Eui Hyuk Jung; Jeon, N. J.; Kim, Y. C.; Lee, D. U.; Shin, S. S.; Seo, J.; Kim, E. K.; Noh, J. H.; Seok, S. I. Iodide Management in Formamidinium-Lead-Halide–Based Perovskite Layers for Efficient Solar Cells. *Science* **2017,** *356*, 1376-1379.

61. Zhao, W.; Xu, J.; He, K.; Cai, Y.; Han, Y.; Yang, S.; Zhan, S.; Wang, D.; Liu, Z.; Liu, S. A Special Additive Enables All Cations and Anions Passivation for Stable Perovskite Solar Cells with Efficiency over 23. *Nano-Micro Lett.* **2021,** *13*, 169.

62. Lee, J. W.; Tan, S.; Seok, S. I.; Yang, Y.; Park, N. G. Rethinking the A Cation in Halide Perovskites. *Science* **2022,** *375*, eabj1186.

63. Gao, L.; Spanopoulos, I.; Ke, W.; Huang, S.; Hadar, I.; Chen, L.; Li, X.; Yang, G.; Kanatzidis, M. G. Improved Environmental Stability and Solar Cell Efficiency of (MA,FA)PbI_3 Perovskite Using a Wide-Band-Gap 1D Thiazolium Lead Iodide Capping Layer Strategy. *ACS Energy Lett.* **2019,** *4*, 1763-1769.

64. Yuan, Z.; Zhou, C.; Tian, Y.; Shu, Y.; Messier, J.; Wang, J. C.; van de Burgt, L. J.; Kountouriotis, K.; Xin, Y.; Holt, E.; Schanze, K.; Clark, R.; Siegrist, T.; Ma, B. One-Dimensional Organic Lead Halide Perovskites with Efficient Bluish White-Light Emission. *Nat. Commun.* **2017,** *8*, 14051.

65. Huang, Y.; Li, L.; Liu, Z.; Jiao, H.; He, Y.; Wang, X.; Zhu, R.; Wang, D.; Sun, J.; Chen, Q.; Zhou, H. The Intrinsic Properties of $FA_{(1-x)}MA_xPbI_3$ Perovskite Single Crystals. *J. Mater. Chem. A* **2017,** *5*, 8537-8544.

66. Leijtens, T.; Eperon, G. E.; Barker, A. J.; Grancini, G.; Zhang, W.; Ball, J. M.; Kandada, A. R. S.; Snaith, H. J.; Petrozza, A. Carrier Trapping and Recombination: The Role of Defect Physics in Enhancing the Open Circuit Voltage of Metal Halide Perovskite Solar Cells. *Energy Environ. Sci.* **2016,** *9*, 3472-3481.

67. Qin, C.; Jiang, Z.; Zhou, Z.; Liu, Y.; Jiang, Y. Excitation Wavelength and Intensity-Dependent Multiexciton Dynamics in $CsPbBr_3$ Nanocrystals. *Nanomaterials* **2021,** *11*, 463.

68. Bi, C.; Wang, S.; Wen, W.; Yuan, J.; Cao, G.; Tian, J. Room-Temperature Construction of Mixed-Halide Perovskite Quantum Dots with High Photoluminescence Quantum Yield. *J. Phys. Chem. C* **2018,** *122*, 5151-5160.

69. Wang, H.; Bian, H.; Jin, Z.; Zhang, H.; Liang, L.; Wen, J.; Wang, Q.; Ding, L.; Liu, S. F. Cesium Lead Mixed-Halide Perovskites for Low-Energy Loss Solar Cells with Efficiency Beyond 17%. *Chem. Mater.* **2019,** *31*, 6231-6238.

70. Singh, M.; Ho, I. H.; Singh, A.; Chan, C.-W.; Yang, J.-W.; Guo, T.-F.; Ahn, H.; Tung, V.; Chu, C. W.; Lu, Y.-J. Unveiling Ultrafast Carrier Extraction in Highly Efficient 2D/3D Bilayer Perovskite Solar Cells. *ACS Photonics* **2022,** *9*, 3584-3591.

71. Abate, S. Y.; Wu, W.-T.; Pola, S.; Tao, Y.-T. Compact TiO_2 Films with Sandwiched Ag Nanoparticles as Electron-Collecting Layer in Planar type Perovskite Solar Cells: Improvement in Efficiency and Stability. *RSC Adv.* **2018,** *8*, 7847-7854.

72. Christians, J. A.; Manser, J. S.; Kamat, P. V. Best Practices in Perovskite Solar Cell Efficiency Measurements. Avoiding the Error of Making Bad Cells Look Good. *J. Phys. Chem. Lett.* **2015,** *6*, 852-7.

TOC

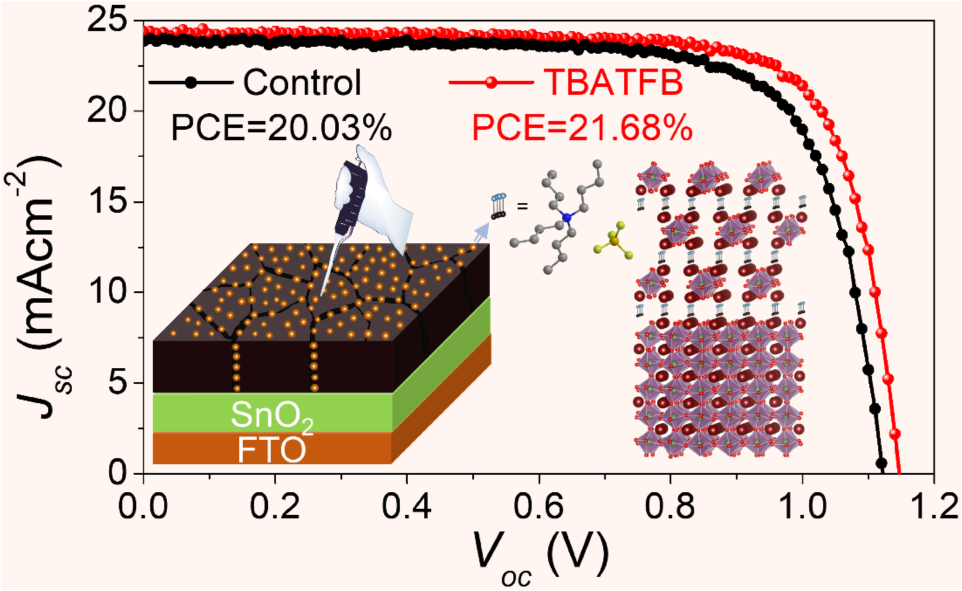

Control
PCE=20.03%
TBATFB
PCE=21.68%
SnO$_2$
FTO
=
J_{sc} (mAcm^{-2})
V_{oc} (V)
0
5
10
15
20
25
0.0
0.2
0.4
0.6
0.8
1.0
1.2